SCIENTIFIC REPORTS

OPEN

SUBJECT AREAS:
FUEL CELLS
MECHANICAL AND STRUCTURAL PROPERTIES AND DEVICES
STRUCTURAL PROPERTIES
NANOPARTICLES

Received
7 November 2013

Accepted
17 January 2014

Published
5 February 2014

Correspondence and requests for materials should be addressed to S.C.M. (msc@whut.edu.cn)

Nano Conductive Ceramic Wedged Graphene Composites as Highly Efficient Metal Supports for Oxygen Reduction

Peng Wu, Haifeng Lv, Tao Peng, Daping He & Shichun Mu

State Key Laboratory of Advanced Technology for Materials Synthesis and Processing, Wuhan University of Technology, Wuhan 430070, China.

A novel conductive ceramic/graphene nanocomposite is prepared to prohibit the re-stacking of reduced graphene oxide (RGO) by wedging zirconium diboride (ZrB_2) nanoparticles (NPs) into multiple layer nanosheets using a simple solvothermal method. Surprisingly, the RGO/ZrB_2 nanocomposite supported Pt NPs shows very excellent catalytic activity. Its electrochemical surface area (ECSA) is up to 148 m^2g^{-1} (very approaches the geometry surface area of 155 m^2g^{-1}), much greater than that of the previous report (usually less than 100 m^2g^{-1}). The mass activity is as high as 16.8 A/g^{-1}, which is almost 2 times and 5 times that of Pt/RGO (8.6 A/g^{-1}) and Pt/C (3.2 A/g^{-1}), respectively, as benchmarks. Moreover, after 4000 cycles the catalyst shows only 61% of ECSA loss, meaning a predominantly electrochemical stability. The remarkably improved electrochemical properties with much high Pt utilization of the new catalyst show a promising application in low temperature fuel cells and broader fields.

Low temperature fuel cells (LTFCs) are promising electrochemical devices for the direct conversion of chemical energy of hydrogen into electrical work[1]. However, the high cost owing to a low utilization of the noble metal catalyst (i.e., Pt), and the low stability owing to sensitive oxidation of conventional carbon black supports under radically chemical and electrochemical oxidation conditions at cathode for fuel cells[2,3], have seriously hindered the commercialization of LTFCs. Recently, graphene nanosheet (GNS) has attracted a great attention as catalyst supports owing to its unique properties such as very large theoretical specific surface area (2630 $m^2\ g^{-1}$), high electrical conductivity, superior catalytic activity by nitrogen doping or halogen-functionalized, and high chemical and electrochemical stabilities[4–9]. However, due to the strong exfoliation energy of the π-stacked layers in graphite caused by the $\pi-\pi$ interaction[10,11], the 2D GNS readily tends to restack when used as catalyst supports[12]. This directly results in significant reduction of the geometry surface area of support materials, decreasing the ECSA of the noble metal catalyst[13] and heavily hindering the catalytic reaction due to an elevated resistance for the diffusion of reactant species[14]. So far, some attempts have been made to prevent such restacking, including the combination of GNS with other carbon building blocks, such as carbon nanotubes, fullerene, carbon nanospheres and carbon nanofibers[13,15–18]. However, such carbon building blocks increase the complexity of the synthesis process and can be electrochemically oxidized under the harsh work environment of proton exchange membrane fuel cells (PEMFCs).

Hence, chemically inert nano-ceramic materials have attracted much attention as alternative support materials for fuel cell catalysts because of their outstanding oxidation and acid corrosion resistance as well as excellent thermal stability[19,20]. We[21–23] have demonstrated nano-boron carbide (B_4C), nano-silicon carbide (SiC), titanium diboride (TiB_2) as well can act as stable catalyst supports in PEMFCs. However, the electrical conductivity of such ceramics needs to be further improved. Fortunately, zirconium diboride (ZrB_2), with unique metallic conductive nature, has been reported[24] and shows more excellent thermal and electrical conductivities, high corrosion resistance, as well as good thermal stability and mechanical property[25,26]. However, differently from the previously reported GNS/carbon/GNS sandwich architectures by us[13], the presence of a big difference in density between nano-ceramics and graphene, can prevent the nano-ZrB_2 particles from being incorporated into the spacing between the reduced graphene oxide (RGO) layers in liquid solutions. Consequently, as shown in Figure 1a, the nano ZrB_2 particle is expected to be wedged into spacing between the multiple layer RGO (or few-layer RGO stacks) and to form a graphitic network. Instead of the GNS/carbon/GNS sandwich architecture, such unique structure is anticipated to greatly increase the geometry surface area of RGO by prohibiting the restacking and the

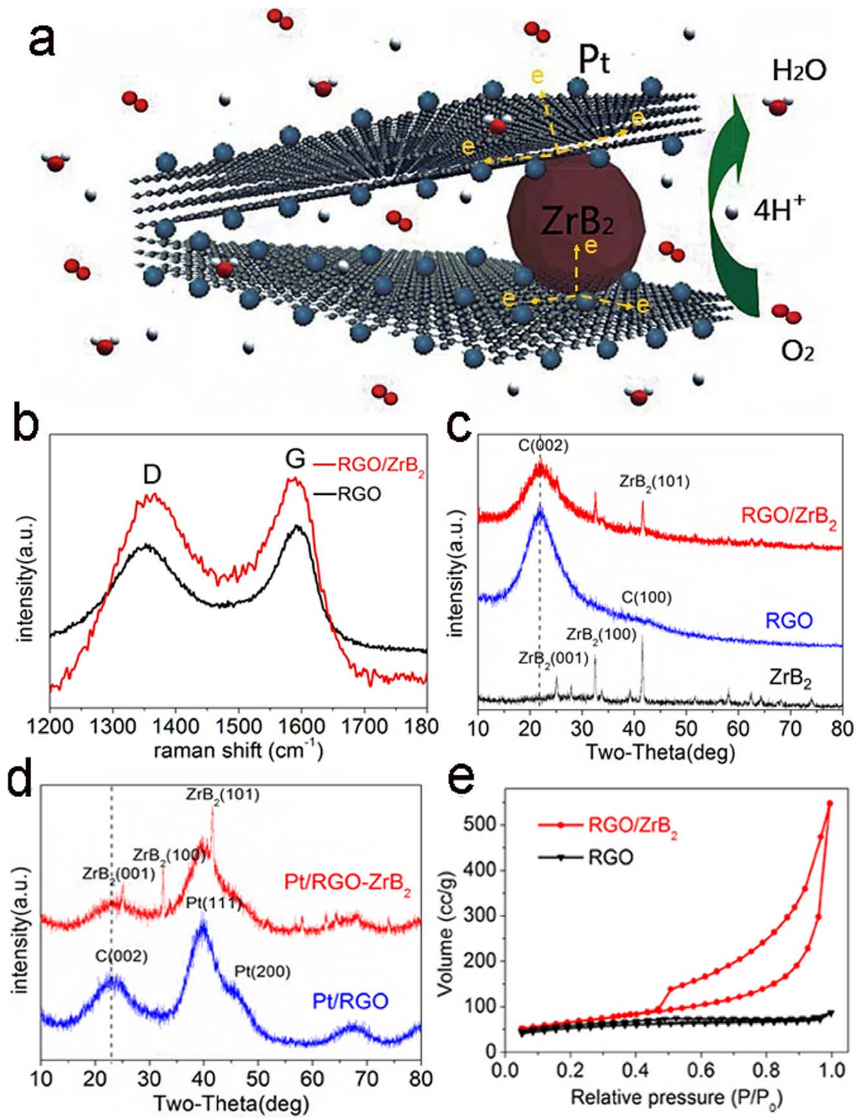

Figure 1 | (a) A nano-ZrB_2 wedged RGO composite as a support of Pt nanoparticles with enhanced catalytic activity towards the oxygen reduction, (b) Raman spectra, (c) (d) XRD spectra of RGO, RGO/ZrB_2, ZrB_2 and Pt/RGO, Pt/RGO-ZrB_2, (e) nitrogen adsorption-desorption isotherms of RGO and RGO/ZrB_2.

crumpled surfaces being formed, and to facilitate the permeation of electrolyte and the transport of both electrons/protons and reaction species in GNS stacks, thus improving the electrochemical property of Pt NPs.

Results

Figure 1 b displays the Raman spectra of RGO and RGO/ZrB_2, the peaks at 1348 and 1585 cm^{-1} can be ascribed to the D and G bands of graphene. The D band corresponds to defects and staging disorder in the curved GNS, while the G band is related to the graphitic hexagon-pinch mode (C sp^2 atoms)[27,28]. The ratios of the intensities of D band to G band (ID/IG) for RGO and RGO/ZrB_2 are 0.88 and 0.93, respectively. The increased D peak of RGO/ZrB_2 indicates an increase in disordered structures after the wedging of nano-ZrB_2 into few-layer GNS stacks. As shown in Figure 1c, a duller and broader carbon (002) XRD diffraction peak appears for RGO/ZrB_2, which also indicates a lower graphitic ordered structure of graphene. The lower graphitization index of RGO indicates a lower ordered graphitic structure. This is consistent with the Raman spectra (Figure 1b).

Moreover, instead of a shift of peak (002) of GNS sandwiched by carbon building blocks to a lower angle[13,29,30] which indicates an increased spacing between GNS layers, the RGO/ZrB_2 nanocomposite does not show any shift at the same peak site, demonstrating the interlayer spacing of GNS cannot be altered by wedging the nano-ZrB_2. This result indicates that the nano-ZrB_2 particle can only be wedged into the RGO stacks consisted of multiple layer nanosheets, which is in good agreement with our previous assumption that the presence of the big difference in density between nano-ceramics and graphene prevents the nano-ceramic from being inserted into the GNS layers in liquid solutions. In order to investigate the unique architecture of samples, SEM and TEM observations were further developed (Figure 2, 3 and Figure S1). It can be seen that the pristine RGO with a layered structure has typically crumpled surfaces. At the same time, due to the $\pi-\pi$ interaction, the 2D RGO nanosheet tends to re-stack (Figure 2a, b and Figure S1a). In contrast, after the wedging of nano-ZrB_2 into the RGO stacks in the RGO/ZrB_2 nanocomposites, the RGO stacks are unfolded in terms of nano-wedge effect of ZrB_2 NPs (Figure 2c, d and Figure S1b). Figure 3 shows HRTEM images of the Pt/RGO-ZrB_2, Pt/RGO and Pt/C catalysts. It is interesting that after the platinization the typically crumpled surface of Pt/RGO and unfolded structure of Pt/RGO-ZrB_2 still remains (Figure 3a, c and Figure S1c, d). As shown in Figure 3a

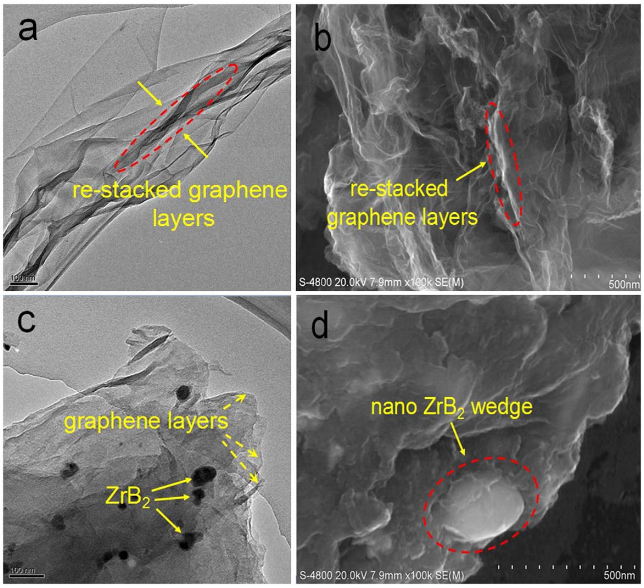

Figure 2 | TEM image of RGO (a), RGO/ZrB_2 (c) and SEM image of RGO (b), RGO/ZrB_2 (d).

and b, the average particle size of Pt NPS is 2.56 nm with uniform dispersion on RGO surfaces because of the presence of abundant oxygen-containing functional groups on its surfaces. Figure 3c shows that the Pt NPs are homogeneously dispersed on RGO/ZrB_2 nanocomposites. The lattice spacing of Pt and ZrB_2 is ~0.22 and ~0.216 nm, corresponding to Pt (1 1 1) and ZrB_2 (1 0 1), respectively. The average particle size of the nano-ZrB_2 is 45 nm and the Pt NPs have a very narrow particle size with diameters in the range of 1 to 3 nm (~1.89 nm in average) (Figure 3d), which is consistent with the result from XRD patterns as shown in Figure 1d. The Pt volume-averaged particle size of the Pt/RGO-ZrB_2 and Pt/RGO, calculated by the Scherrer equation[31] using the full width at half maximum of the (220) peak, is 1.85 and 2.45 nm, respectively. Moreover, the Pt/C catalyst has a Pt particle size of 2.86 nm (Figure 3e and f).

Figure 4a exhibits CV curves of the catalysts recorded at room temperatures from 0 to 1.2 V at a scan rate of 50 mV/s. Significantly, our Pt/RGO-ZrB_2 catalyst reveals a unusually high ECSA (148 $m^2 g^{-1}$), which increases by 43% and 62% in comparison with the Pt/RGO (103 $m^2 g^{-1}$) and Pt/C (63 $m^2 g^{-1}$) catalysts (Figure 4 a and b). Such high ECSA value very approaches the theoretical geometry surface area of 154 $m^2 g^{-1}$ of Pt NPs (Figure 4c), which is much greater than that the previous reported (Figure 4c) and also possesses a remarkably high utilization rate of Pt compared with other catalysts (Figure 4d)[11,13,16,19,31–34]. Furthermore, it can be seen that the Pt/RGO-ZrB_2 catalyst has the higher half-wave potential (0.85 V) than that of Pt/RGO (0.8 V) and Pt/C (0.79 V) catalysts (Figure 4e). The kinetic current can be calculated from the ORR polarization curve according to the Koutecky-Levich equation[35]. As shown in Figure 4f, the mass activity of Pt/RGO-ZrB_2 (16.8 mA mg^{-1}) is 1.9 and 5.2 times that of Pt/RGO (8.6 mA mg^{-1}) and Pt/C (3.2 mA mg^{-1}), respectively, indicating greatly improved ORR activity achieved using the RGO/ZrB_2 nanocomposite as the Pt catalyst support. In addition, Figure. S2a presents the current potential curves of the Pt/RGO-ZrB_2 at various rotating rates from 400 to 1600 rpm, by which the Koutecky-Levich (K-L) curves at a variety of potentials were plotted (Figure. S2b). It can be seen that the K-L plots have very similar slopes, and the average electron transfer number is 3.96 calculated by the slopes, demonstrating that our catalyst has a four-electron transfer pathway.

The chronoamperometric i-t curves during the first 8 h electrochemical oxidation are shown in Figure 5a. The minimum corrosion current of nano-ZrB_2 among the supports (Vulcan XC-72, RGO, ZrB_2 and RGO/ZrB_2,) is achieved. Importantly, the RGO/ZrB_2 exhibits a very lower corrosion current than Vulcan XC-72 and RGO under the same conditions, indicating that the resistance to electrochemical oxidation of RGO/ZrB_2 is much enhanced over the pure RGO. Furthermore, the accelerated durability test (ADT) of the catalysts was carried out by continuously applying linear potential sweeps. As shown in Figure S3, both the catalysts exhibit a decrease in the hydrogen adsorption regions after the ADT, indicating a loss of ECSA with repeated potential cycling. Normalized with the initial one, the loss of the ECSA is plotted as a function of cycle numbers (Figure 5b). It is interesting that, after 4000 cycles the ECSA loss of

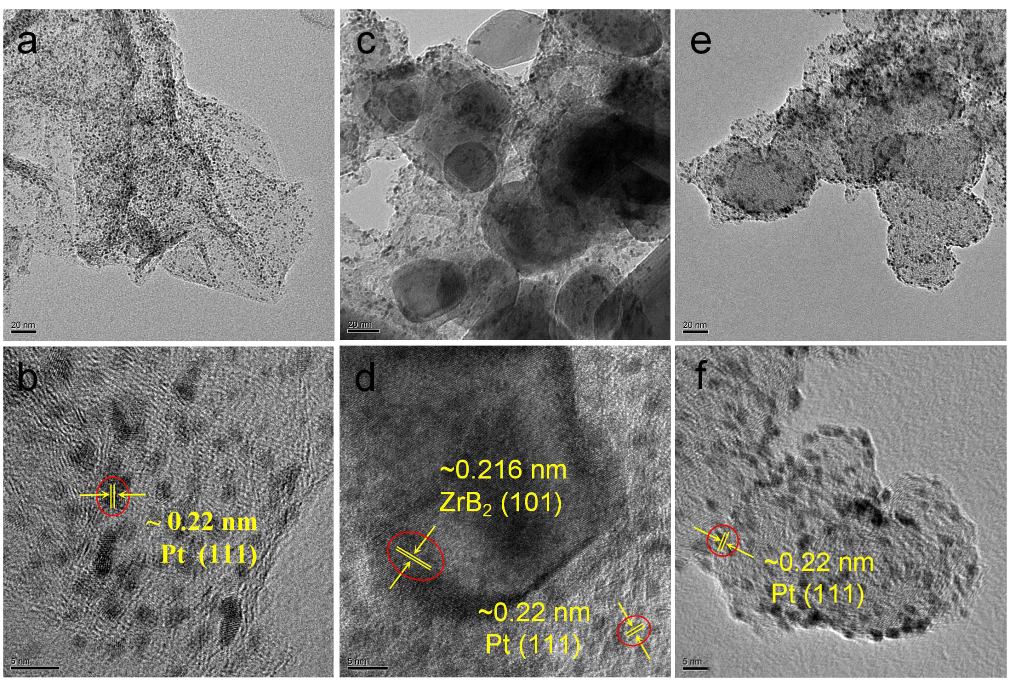

Figure 3 | TEM images of Pt nanoparticles supported on RGO (a, b), RGO/ZrB_2 (c, d) and C (e, f).

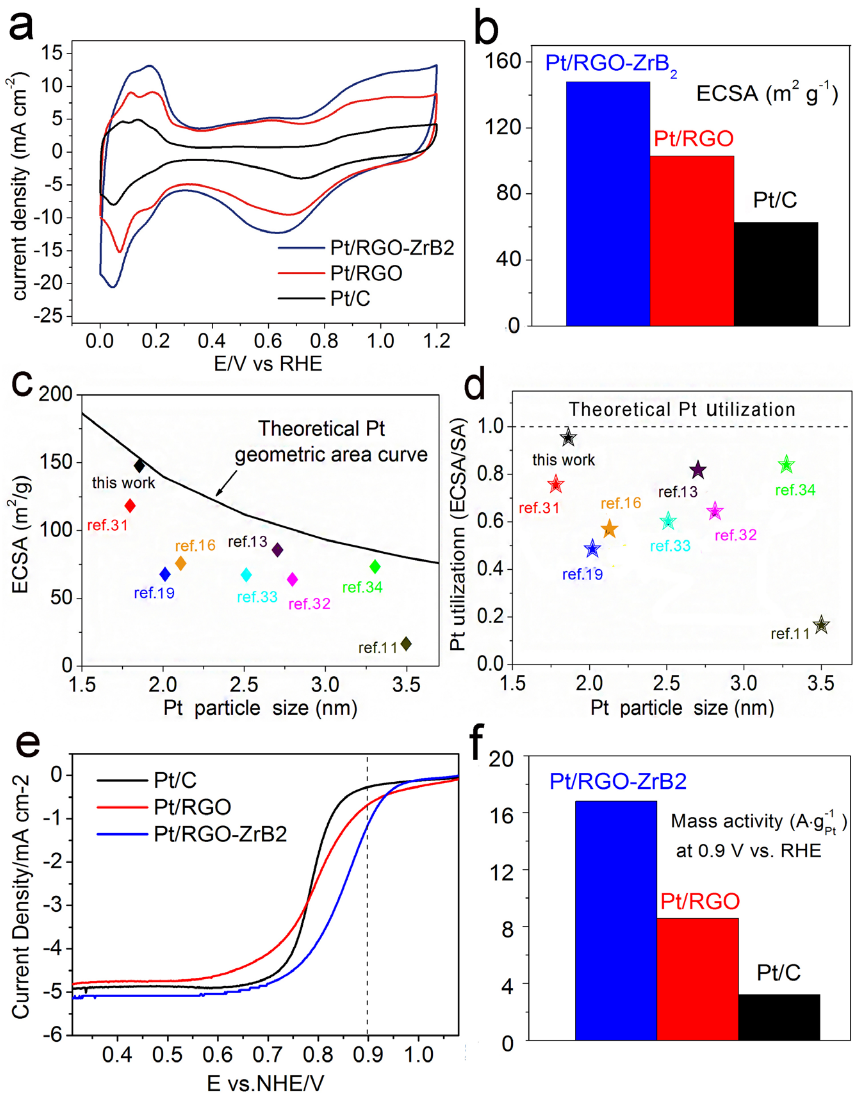

Figure 4 | CV curves (a), ECSA (b) of the Pt/RGO/ZrB_2, Pt/RGO and Pt/C catalyst, the ECSA (c) and Pt utilization (d) compared with other relevant data recently reported in the literature, current-potential polarized curves for ORR (e), and the mass activities at 0.9 V (f).

the commercial Pt/C and Pt/RGO is up to 87% and 68%, respectively, whereas the Pt/RGO-ZrB_2 is only 61%, which clearly indicates that the Pt/RGO-ZrB_2 is more stable compared with the Pt/RGO and Pt/C under the same testing conditions. This result is consistent with the result from the chronoamperometric i-t curves (Figure 5a) that the resistance to electrochemical oxidation of RGO/ZrB_2 is much better than RGO and XC-72. The particle size distribution of the Pt NPs was obtained from HRTEM images (Figure 5 and Figure S4) by measuring more than 150 particles in each sample. In the case of the Pt/RGO catalyst, a massive decrease of Pt NPs can be found in Figure 5c and Figure S4a, b where the average particle size increases from 2.6 to 6.5 nm (Figure 5d). In contrast, relative low agglomeration of Pt NPS occurs for the Pt/RGO-ZrB_2 (Figure 5e and Figure S4c, d) with a more sluggish increment in the particle size from 1.9 to 5.5 nm (Figure 5f). As a reference, serious agglomeration of Pt NPS, from 2.9 to 7.3 nm, for the Pt/C catalyst appears (Figure 5g, h and Figure S4e, f).

Discussion

The enhanced electrocatalytic activity can be derived from the nano-wedge effect of ZrB_2: 1) the enlarged spacing between few-layer RGO stacks due to the wedging of nano-ZrB_2 particles with a good conductive property, leading to improved diffusion of electrolyte and transport of the reaction species. 2) the unfolded structure exalted by nano ZrB_2 due to a higher density than carbon, allowing RGO a greater geometry surface area, which promotes the uniform dispersion of noble metal NPs with a small particle size in average. As shown in Figure 1e, the BET surface area of the RGO/ZrB_2 composite is about 330 $m^2 g^{-1}$, which is almost two times of the RGO (171 $m^2 g^{-1}$). However, for the simple mixture of RGO and ZrB_2 by hand milling, the surface area of the composite is only 119.4 $m^2 g^{-1}$ (Figure S5) which is far less than our RGO/ZrB_2 composite. Thus, the greatly increased surface area of the RGO/ZrB_2 support leads to the higher dispersion and the narrower size distribution of Pt NPs in comparison with the pure GNS support. 3) the presence of the nano ZrB_2 wedge does not obviously affect the electron transport due to the excellent conductive property of ZrB_2 ceramic (the charge transfer resistance (R_{ct}) is 38.68 Ω). As shown in Figure S6a, although the R_{ct} of the RGO-ZrB_2 composite (28.69 Ω) is little lower than that of graphene (25.97 Ω) and carbon black (23.19 Ω), after platinization the R_{ct} of the Pt/RGO-ZrB_2 is 5.23 Ω which is very close to Pt/RGO (4.19 Ω) and Pt/C (3.41 Ω) due to the excellent conductivity of Pt metal (Figure S6b).

These results also show that the presence of the stable ZrB_2 nano-wedge between the RGO stack endows the new support with a higher stability, effectively preventing the RGO stack from rapidly re-stacking

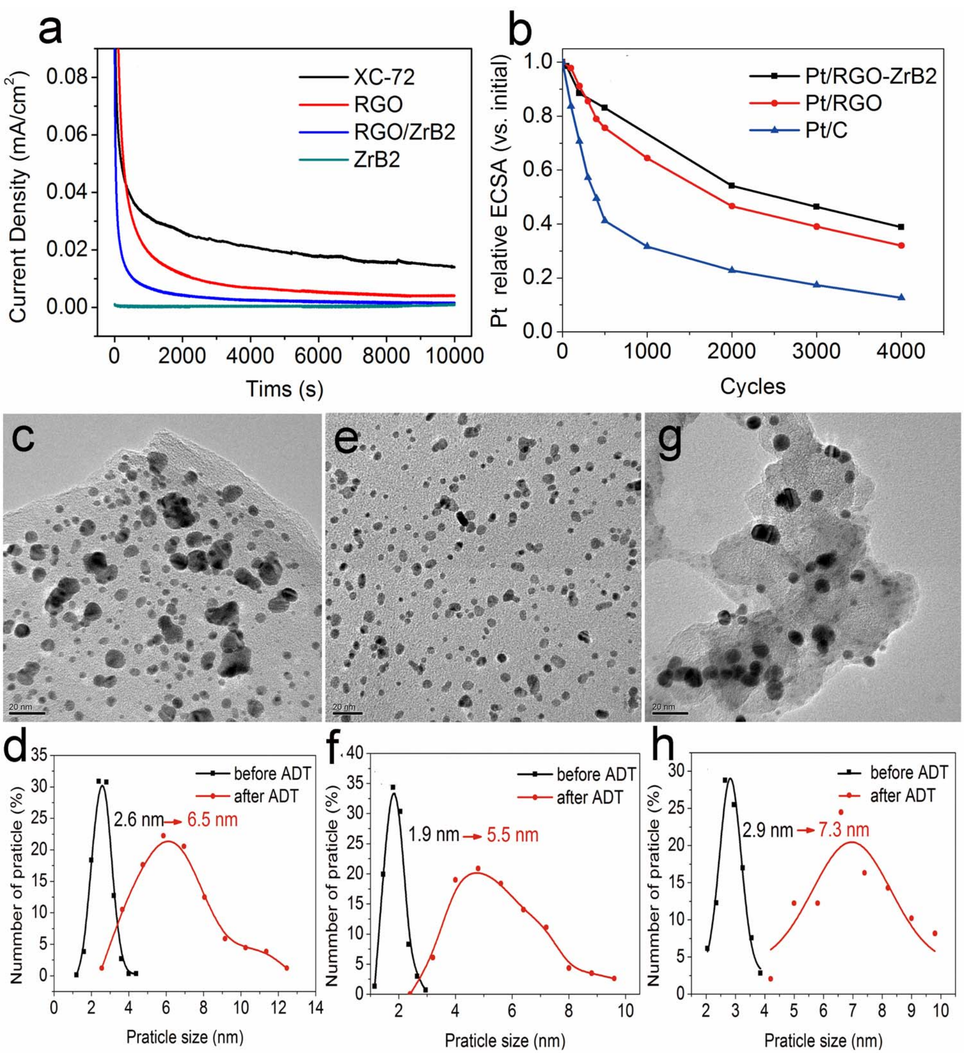

Figure 5 | The chronoamperometric curves after 8 h electrochemical oxidation of XC-72, RGO, RGO/ZrB_2, ZrB_2 (a), changes of ECSA of catalysts related to Pt catalytic surface area with the increased potential cycles (b). TEM image of the Pt/RGO (c), Pt/RGO/ZrB_2 (e) and Pt/C (g) catalysts after ADT. Pt particle size distributions of Pt/RGO (d), Pt/RGO/ZrB_2 (f) and Pt/C (h) before (black) and after (red) ADT.

during electrochemical acceleration. In contrast, the pristine 2D RGO nanosheets are susceptible to the π−π interaction, and tend to re-stack, leading to typically crumpled surfaces formed on RGO during acceleration. The crumpled surfaces can further veil the active sites of Pt and separate electrolyte from the reaction system, accelerating inactivation of Pt when used as catalyst supports. Moreover, compared with a smooth RGO surface, RGO-ZrB_2 is richer in kinks and traps, which provides more nucleation sites for migrating Pt species (atoms or clusters) and re-collects more Pt species which would otherwise combine into larger particles or dissolve into the electrolyte[15].

In summary, we demonstrate that the nano-ZrB_2 wedged graphene composite supported Pt catalyst can achieve excellent electrocatalytic activity and high stability in comparison with the pristine graphene supported Pt catalyst and the commercial Pt/C catalyst, although it has a very different architecture from the conventional GNS/carbon/GNS sandwich building block. To compare the building block[13,14], the nano-ZrB_2 wedged sample shows remarkably high ECSA and utilization rate of Pt, which can be ascribed to the wedge effect of ZrB_2 nanoparticles and the unique architecture of the RGO/ZrB_2 nanocomposite that greatly decreases the re-stacking and the crumpled surfaces of graphene nanosheets. The novel catalyst arises a promising application in low temperature fuel cells.

Methods

The process of synthesizing GO/ZrB_2 nanocomposite and the subsequent deposition of Pt NPs on RGO/ZrB_2 and RGO is depicted in Scheme S1. Graphene oxide (GO) was prepared by the modified Hummers method[36]. First of all, seventy milligram of the GO was added to EG solution and followed by ultrasonic treatment for 1 h. After that, Thirty milligram of ZrB_2 with an average particle size of 45 nm and a BET surface area of 38 m^2/g was mixed with GO aqueous suspension, afterwards, the mixture was allowed to vigorous stirring about 4 h, and then the samples was completely dried by lyophilisation, and then the resultant GO/ZrB_2 nanocomposite was achieved. Pt NPs were deposited on the obtained RGO/ZrB_2 by an ethylene glycol (EG) reduction method. One hundred milligram of the GO/ZrB_2 nanocomposite was added to EG solution and followed by ultrasonic treatment for 30 min, and then transferred into a round bottom flask. Afterwards, the Pt precursor $H_2PtCl_6 \cdot 6H_2O$ (Sinopharm Chemical Reagent Co., Ltd.) solution was added dropwise into the GO/ZrB_2 suspension under vigorous stirring. The pH of the solution was adjusted to 10–12 using 1.0 M of NaOH aqueous solution, and then the mixture was heated under reflux at 150°C for 3–4 h to ensure the Pt NPs were completely obtained and the GO was reduced to RGO. After stirring overnight, the mixture was filtered and washed with deionized water. The obtained catalyst was dried in a vacuum oven at 80°C for 8 h. For comparison purposes, RGO supported Pt catalysts (Pt/RGO) were synthesized following a similar procedure and commercial Pt/C catalyst (30 wt.% Pt supported on carbon black) was purchased from E-TEK.

The microstructures of the composite support and catalyst were analyzed using the JEOL 2100 high-resolution transmission electron microscope (HRTEM),the JEOL JEM 6700 scanning electron microscope (SEM) operating at 10 kV, Raman spectroscopy was carried out on a Renishaw using the Ar ion laser with an excitation wavelength of 514.5 nm. N_2 adsorption-desorption isotherms were recorded at 77 K with a Micromeritics ASAP 2020 Brunauer-Emmett-Teller (BET) analyzer.and X-ray diffraction with Cu Kα source ($\lambda = 1.54056$ Å) at a scan rate of 5° min^{-1} from 10° to 80°. The average crystallite size (D) of Pt nano-particles can be obtained according to the Scherrer equation[37] using the Pt (220) peak. The electrocatalytic performance of the catalysts was tested with a computer controlled Autolab PGSTAT 30 potentiostat (Eco Chemie B.V, Holland) with a three-electrode cell setup. A platinum electrode was the counter electrode, while a Hg/Hg_2Cl_2 electrode was the reference electrode. All potentials measured were referred to the normal hydrogen electrode (NHE). Electrolyte solutions (0.5 M H_2SO_4 solution) were deaerated by high purity nitrogen for 30 min prior to any electrochemical measurements. 6 mg of sample was dispersed in 1 mL of deionized water and then mixed with 100 uL 5 wt% perfluorosulfonic acid (PSFA) Nafion (DuPont Co., Ltd.) solution and coated on a mirror-polished glassy carbon disk electrode as working electrode. In the chronoamperometric i-t test, a constant 1.2 V voltagewas applied in the electrochemical oxidation experiments. An electrochemical accelerated durability test(ADT)was conducted by cyclic voltammograms (CVs) between 0.6 and 1.2 V for 4000 cycles. Before and after the ADT, CVs were recorded from 0 to 1.2 V at a scan rate of 50 mVs^{-1}. The electrochemical surface area (ECSA) was calculated from the reported equation[38]. In addition, the oxygen reduction reaction (ORR) activity of the catalysts was performed in O_2 saturated 0.5 M H_2SO_4 on a rotating disk electrode (RDE) system. Polarization curves were obtained at room temperature with a scan rate of 10 mVs^{-1} and a rotation rate of 1600 rpm, recorded from 1.1 to 0.2 V. The kinetic current can be calculated from the ORR polarization curve according to the Koutecky–Levich equation[35]. Electrochemical impedance spectroscopy (EIS) was measured by an EC-lab SP300 frequency response analyzer and the frequency ranged from 1 MHz to 1 Hz.

1. Steele, B. C. H. & Heinzel, A. Materials for fuel-cell technologies. *Nature.* **414**, 345–352 (2001).
2. Cheng, N. C., Mu, S. C., Pan, M. & Edwards, P. P. Improved lifetime of PEM fuel cell Catalysts through polymer stabilization. *Electrochem. Commun.* **11**, 1610–1614 (2009).
3. Maass, S., Finsterwalder, F., Frank, G., Hartmann, R. & Merten, C. Carbon support oxidation in PEM fuel cell cathodes. *J. Power Sources.* **176**, 444–451 (2008).
4. Zhu, Y. W. *et al.* Graphene and graphene oxide: synthesis, properties, and applications. *Adv. Mater.* **22**, 3906–3924 (2010).
5. Lee, C., Wei, X. D., Kysar, J. W. & Hone, J. Measurement of the elastic properties and intrinsic strength of monolayer graphene. *Science.* **321**, 385 (2008).
6. Jeon, I. Y. *et al.* Direct nitrogen fixation at the edges of graphene nanoplatelets as efficient metal-free electrocatalysts for energy conversion. *Sci. Rep.* **3**, DOI: 10.1038/srep02260 (2013).
7. Jeon, I. Y. *et al.* Facile, scalable synthesis of edge-halogenated graphene nanoplatelets as efficient metal-free eletrocatalysts for oxygen reduction reaction. *Sci. Rep.* **3**, DOI:10.1038/srep01810 (2013).
8. Balandin, A. A. *et al.* Superior thermal conductivity of single-layer graphene. *Nano Lett.* **8**, 902–907 (2008).
9. Li, H. L. *et al.* Oxidation Stability of Nanographite Materials. *Adv. Energy Mater.* **3**, 1176–1179 (2013).
10. Chen, D.,Tang, L. H. & Li, J. H. Graphene-based materials in electrochemistry. *Chem. Soc. Rev.* **39**, 3157–3180 (2010).
11. Xiao, Y. P. *et al.* Hanging Pt hollow nanocrystal assemblies on graphene resulting in an enhanced electrocatalyst. *Chem. Commun.* **48**, 10331–10333 (2012).
12. Si, Y. & Samulski, E. T. Exfoliated graphene separated by platinum nanoparticles. *Chem. Mater.* **20**, 6792–6797 (2008).
13. He, D. P., Cheng, K., Peng, T., Pan, M. & Mu, S. C. Graphene/carbon anospheres sandwich supported PEM fuel cell metal nanocatalysts with remarkable high activity and stability. *J. Mater. Chem. A.* **1**, 2126–2132 (2013).
14. Li, Y. J. *et al.* Stabilization of High-Performance Oxygen Reduction Reaction Pt Electrocatalyst Supported on Reduced Graphene Oxide/Carbon Black Composite. *J. Am. Chem. Soc.* **134**, 12326–12329 (2012).
15. Fan, Z. J. *et al.* A Three-Dimensional Carbon Nanotube/Graphene Sandwich and Its Application as Electrode in Supercapacitors. *Adv. Mater.* **22**, 3723–3728 (2010).
16. Li, Y. L., Hu, F. P., Wang, X. & Shen, P. K. Anchoring metal nanoparticles on hydrofluoric acid treated multiwalled carbon nanotubes as stable electrocatalysts. *Electrochem. Commun.* **10**, 1101–1104 (2008).
17. Lei, Z. B., Christov, N. & Zhao, X. S. Intercalation of mesoporous carbon spheres between reduced graphene oxide sheets for preparing high-rate supercapacitor electrodes. *Energy Environ. Sci.* **4**, 1866–1873 (2011).
18. Fan, Z. J. *et al.* Nanographene-constructed carbon nanofibers grown on graphene sheets by chemical vapor deposition: High-performance anode materials for lithium ion batteries. *ACS Nano.* **5**, 2787–2794 (2011).
19. Kou, R. *et al.* Stabilization of electrocatalytic metal nanoparticles at metal– metal oxide– graphene triple junction points. *J. Am. Chem. Soc.* **133**, 2541–2547 (2011).
20. Huang, S. Y., Ganesan, P., Park, S. & Popov, B. N. Development of a titanium dioxide-supported platinum catalyst with ultrahigh stability for polymer electrolyte membrane fuel cell applications. *J. Am. Chem. Soc.* **131**, 13898–13899 (2009).
21. Lv, H. F., Peng, T., Wu, P., Pan, M. & Mu, S. C. Nano-boron carbide supported Platinum catalysts with much enhanced methanol oxidation activity and CO tolerance. *J. Mater. Chem.* **22**, 9155–9160 (2012).
22. Lv, H. F., Mu, S. C., Cheng, N. C. & Pan, M. Nano silicon carbide supported catalysts for PEM fuel cells with high electrochemical stability and improved performance by addition of carbon. *Appl. Catal. B.* **100**, 190–196 (2010).
23. Yin, S. B. *et al.* highly stable catalyst for PEM fuel cell based on durable titanium diboride support and polmer stabilization. *Appl. Catal. B.* **93**, 233–240 (2010).
24. Fahrenholtz, W. G., Hilmas, G. E., Talmy, I. G. & Zaykosk, J. A. Refractory diborides of zirconium and hafnium. *J. Am. Ceram. Soc.* **90**, 1347–1364 (2007).
25. Li, R. X., Zhang, Y., Lou, H. J., Li, J. P. & Feng, Z. H. Synthesis of ZrB_2 nanoparticles by sol–gel method. *J. Sol-Gel Sci. Technol.* **58**, 580–585 (2011).
26. Corral, E. L. & Walker, L. S. Improved ablation resistance of C–C composites using zirconium diboride and boron carbide. *J. Eur. Ceram. Soc.* **30**, 2357–2364 (2010).
27. Sprinkle, M. *et al.* First direct observation of a nearly ideal graphene band structure. *Phys. Rev. Lett.* **103**, 226803-6 (2009).
28. Subrahmanyam, K. S., Vivekchand, S. R. C., Govindaraj, A. & Rao, C. N. R. A study of graphenes prepared by different methods: characterization., properties and solubilization. *J. Mater. Chem.* **18**, 1517 (2008).
29. Aurbach, D. *et al.* On the correlation among surface chemistry, 3D structure, morphology, electrochemical and impedance behavior of various lithiated carbon electrodes. *J. Power Sources.* **97–98**, 92–96 (2001).
30. Gong, P. W. *et al.* One-pot sonochemical preparation of fluorographene and selective tuning of its fluorine coverage. *J. Mater. Chem.* **22**, 16950–16956 (2012).
31. Hsin, Y. L., Hwang, K. C. & Yeh, C. T. Poly (vinylpyrrolidone)-modified graphite carbon nanofibers as promising supports for PtRu catalysts in direct methanol fuel cells. *J. Am. Chem. Soc.* **129**, 9999–10010 (2007).
32. Xia, B. Y. *et al.* Sandwich-structured TiO_2–Pt–graphene ternary hybrid electrocatalysts with high efficiency and stability. *J. Mater. Chem.* **22**, 16499–16505 (2012).
33. Nethravathi, C., Anumol, E. A., Rajamathi, M. & Ravishankar, N. Highly dispersed ultrafine Pt and PtRu nanoparticles on graphene: formation mechanism andelectrocatalytic activity. *Nanoscale.* **3**, 569–571 (2011).
34. Ho, V. T. T., Pan, C. J., Rick, J., Su, W. N. & Hwang, B. J. Nanostructured $Ti_{0.7}Mo_{0.3}O_2$ Support Enhances Electron Transfer to Pt: High-Performance Catalyst for Oxygen Reduction Reaction. *J. Am. Chem. Soc.* **133**, 11716–11724 (2011).
35. Lim, B. *et al.* Pd-Pt bimetallic nanodendrites with high activity for oxygen reduction. *Science.* **324**, 1302–1305 (2009).
36. Hirata, M., Gotou, T., Horiuchi, S., Fujiwara, M. & Ohba, M. Thin-film particles of graphite oxide 1: High-yield synthesis and flexibility of the particles. *Carbon.* **42**, 2929–2937 (2004).
37. Radmilovic, V., Gasteiger, H. A. & Ross, P. N. Structure and chemical composition of a supported Pt-Ru electrocatalyst for methanol oxidation. *J. Catal.* **154**, 98–106 (1995).
38. Schmidt, T. J. *et al.* Characterization of High SurfaceArea Electrocatalysts Using a Rotating Disk Electrode Configuration. *J. Electrochem. Soc.* **145**, 2354–7 (1998).

Acknowledgments

This research was supported by the National Science Foundation of China (No. 51372186), the National Basic Research Development Program of China (973 Program) (No. 2012CB215504) and the Natural Science Foundation of Hubei Province of China (No. 2013CFA082).

Author contributions

S.M. proposed and supervised the project, S.M. and P.W. designed the experiments, P.W. performed experiments under the help of H.L., D.H., T.P. and S.M. and P.W. and S.M. analysed data and wrote the manuscript. All the authors participated in discussions of the research.

Additional information

Supplementary information accompanies this paper at http://www.nature.com/scientificreports

Competing financial interests: The authors declare no competing financial interests.

How to cite this article: Wu, P., Lv, H.F., Peng, T., He, D.P. & Mu, S.C. Nano Conductive Ceramic Wedged Graphene Composites as Highly Efficient Metal Supports for Oxygen Reduction. *Sci. Rep.* **4**, 3968; DOI:10.1038/srep03968 (2014).